Dipole strength distribution
in stable and unstable nuclei.
(P.F. Bortignon)

INT 11/05

D. Sanchi:
G. Colò

PFB

^{208}Pb, ^{120}Sn, ^{132}Sn

$^{18-22}O$

absorption cross section exhibits a strong maximum in the energy region from 10 to 25 MeV, depending on the mass number. An example is shown in Fig. 6-18, while the systematics of the resonance frequencies is given in Fig. 6-19.

The Au cross section shown in Fig. 6-18 has been measured with monoenergetic γ rays produced by the annihilation of positrons in flight. The main mode of decay of the photoexcited nucleus is by neutron emission, since

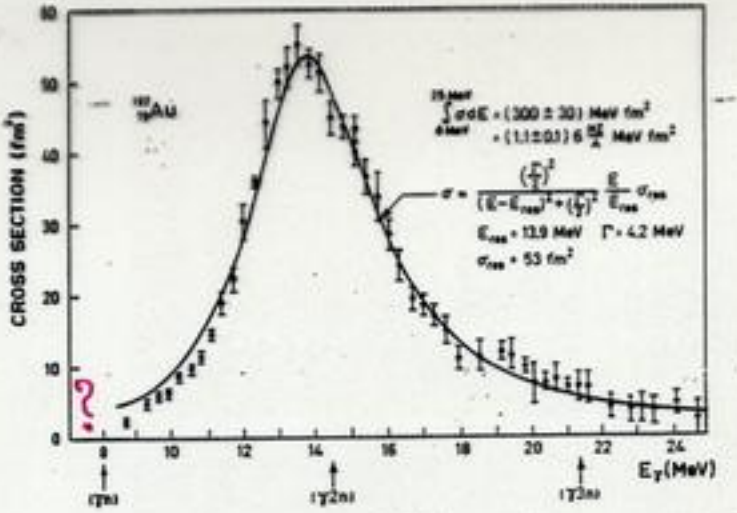

GDR

5-10% of TRK sum rule.

- Y. Suzuki, K. Ikeda and H. Sato, Prog. Th. Phys. 83 (1990)
- P. Van Isacker et al., PRC 45 (1992)

low-lying state?

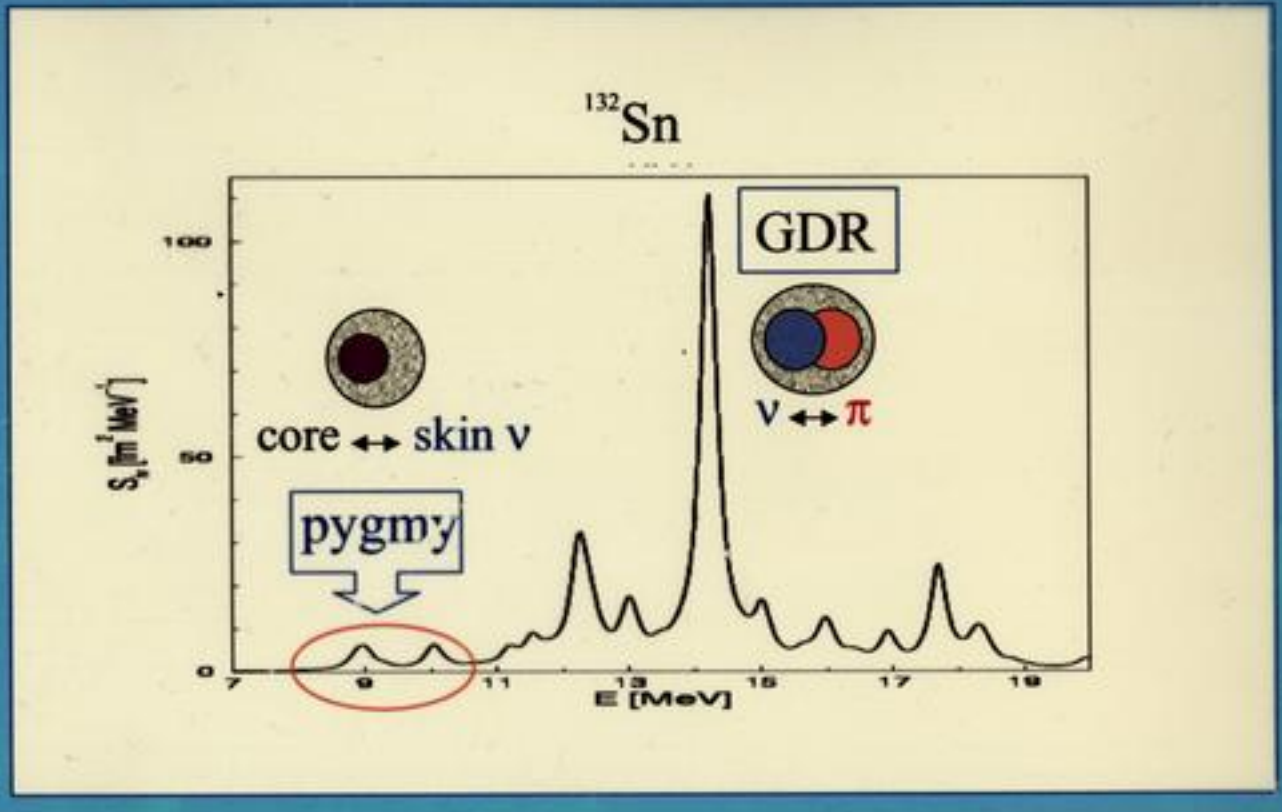

The DC rates are calculated with Eq. (5) for all the nuclei involved in the r-process nucleosynthesis and added incoherently to the damped CN contribution (Eq. (4)) obtained in Section 2. Fig. 5 compares the resulting total (n,γ) rate to the standard rate commonly used in r-process calculations, i.e. deduced from a GDR strength function only. Deviations within a factor of 1000 from the standard GDR predictions can be observed for nuclei relevant to the r-process, i.e such that $1 \lesssim S_n[\mathrm{MeV}] \lesssim 3$. Although for most of the nuclei, the DC and PR effects tend to enhance the neutron capture, the reduced number of available excited states (above and below S_n) in the residual nucleus not only drastically decreases the CN component, but also makes the DC mechanism quite inefficient. For many neutron-rich nuclei, no allowed direct transitions are found, and the direct channel is consequently inhibited [11]. These effects are relatively significant close to the neutron shell closures (especially $N = 82$), and are therefore expected to have an impact on the r-process nucleosynthesis.

4. Impact of the PR and DC on the r-abundance distribution

To illustrate the impact of the PR contribution and DC mechanism on the r-process nucleosynthesis, we consider the simple non-equilibrium canonical model in which a full reaction network is solved for a given set of parameters defining the temperature T of the astrophysical site, its neutron density N_n and the time during which the neutron irradiation takes place τ_{irr}. More details of the r-process model can be found in [15]. The r-process calculations are performed with 3

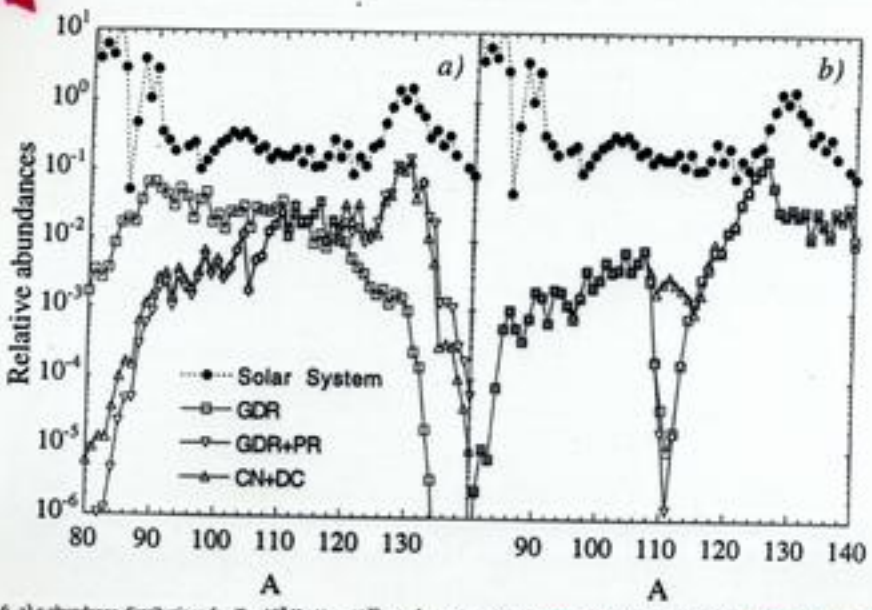

Fig. 6. a) r-abundance distributions for $T = 10^9$ K, $N_n = 10^{20}$ cm^{-3} and $\tau_{irr} = 2.4$ s with 3 different estimates of the neutron capture rate: the standard GDR component, the GDR + PR strength and the damped statistical (CN) plus DC contribution. The top curve corresponds to the solar r-abundances arbitrarily normalized. b) same as a) for $T = 1.5 \times 10^9$ K, $N_n = 10^{28}$ cm^{-3} and $\tau_{irr} = 0.3$ s.

a rather large quadrupole deformation [28]. In stable nuclei, the deformations of the proton and neutron matter distributions are of similar magnitude. An attractive feature in very proton-neutron asymmetric nuclei is the prediction of rather different deformations for protons and neutrons. Nuclear deformations give rise to collective states of low excitation energy, and characteristic vibrational or rotational band structures up to high spins should be observed.

At higher excitation energies, the *giant resonances* are found. Giant resonances are basic excitation modes observed with rather regular patterns in stable nuclei. They are understood as coherent states of vibrational type involving a large number of nucleons inside a nucleus. Giant resonances primarily probe bulk properties of nuclear matter. For instance, the giant monopole resonance has delivered the most precise information on the compressibility of nuclear matter, while the properties of the giant dipole resonance are mainly determined by the nuclear symmetry energy.

A large proton-neutron asymmetry in a nucleus has a significant influence on such collective motions. Their spectral distributions are expected to be much more fragmented than in stable nuclei because the particle-hole energies for protons and neutrons differ considerably from each other. In nuclei with large proton or neutron excess, a distinct separation into isoscalar (protons and neutrons vibrate in phase) and isovector (protons and neutrons vibrate out of phase) modes is no longer adequate. This effect is related to the evolution of skins or halos. The nucleons forming the skin are much less bound than the ones remaining in the core. A new type of vibration may evolve, i.e. a vibration of skin nucleons against core nucleons. Clear evidence for such "soft" collective resonances has not yet been obtained. Low-lying dipole strength exhausting a considerable fraction of the total strength, however, has been found in halo nuclei. This dipole strength which appears just above the neutron separation thresholds, is most likely to be assigned to single-particle transitions which are enhanced due to the strong spatial overlap of the asymptotic part of the valence neutron wavefunction with neutron continuum states.

Recently, a measurement at GSI has shown that low-lying dipole strength evolves systematically with the neutron excess in nuclei which do not exhibit a halo; the results for unstable oxygen isotopes [29] are shown in Figure 1.7. If low-lying dipole strength appears systematically in proton-neutron asymmetric nuclei, the corresponding large photo-neutron cross sections near the neutron separation threshold could have a significant influence on the path of the r-process, see Chapter 1.1.2.3 for further discussion. Giant resonances of other multipolarities are of equal interest. The properties of the giant monopole resonance in exotic nuclei, for instance, would allow the determination of the way in which the nuclear compression modulus evolves with increasing neutron excess. This is important information with regard to the equation of state of neutron matter. Magnetic giant resonances in exotic nuclei are equally important to test nuclear models and, in addition, their knowledge is required in astrophysical model calculations; the latter aspect is discussed in Chapter 1.1.2.3.

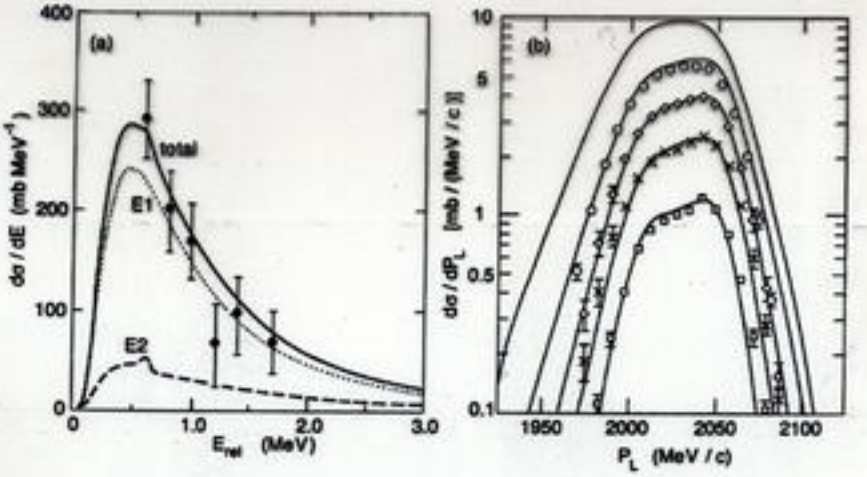

Fig. 1. Decay energy spectrum (a) and longitudinal momentum distributions of ^{7}Be fragments (b) obtained from Coulomb dissociation of ^{8}B on a Pb target at 46.5 and 44 MeV/nucleon, respectively. The data in (a) are from Ref. [7]. The data in (b) are from Ref. [19]; they were obtained for different acceptance angles of the ^{7}Be fragments, namely, 1.5°, 2.4°, 3.5°, and 5.4°. The curves are the results of calculations discussed in the text.

discrepancy with the data at the largest acceptance angle, where the observed asymmetry tends to disappear. This could be caused by nuclear and/or higher-order processes.

A new measurement of the ^{8}B decay energy spectrum has recently been performed [20], which gates on smaller scattering angles of the excited ^{8}B center-of-mass system, i.e., on larger impact parameters. The uncertain influence of nuclear processes has therefore been suppressed. Another advantage is that the relative contribution from E2 transitions is smaller at larger impact parameter. The data have been analyzed by employing the E2 strength that was extracted from the asymmetry of the longitudinal momentum distributions shown in Fig. 1(b). The result of this analysis has not yet been published.

3. RPA linear response of exotic nuclei

3.1. Linear response theory in the coordinate space

The RPA theory of the collective response of nuclei is based on the time dependent HF theory (TDHF). It is formulated in coordinate space [21] as the self-consistent linear response of the HF ground state to an external field. The first step is to determine the induced density in an external field. Let us adopt the time dependent HF field,

$$h(t) = h_0(\rho) + h_1(t) = h_0(\rho) + f(\vec{r})e^{-i\omega t} + f^*(\vec{r})e^{i\omega t}, \tag{13}$$

The 2-quasiparticle components of the GR are coupled with 4-quasiparticle-type states (two quasiparticles plus one density vibration: 2^+, 3^-, 4^+)

This is an extension, to include pairing correlations, of a model developed within the Milano-Orsay collaboration and which has been successful in describing microscopic GR properties [PRC 50 (1994) 1496]

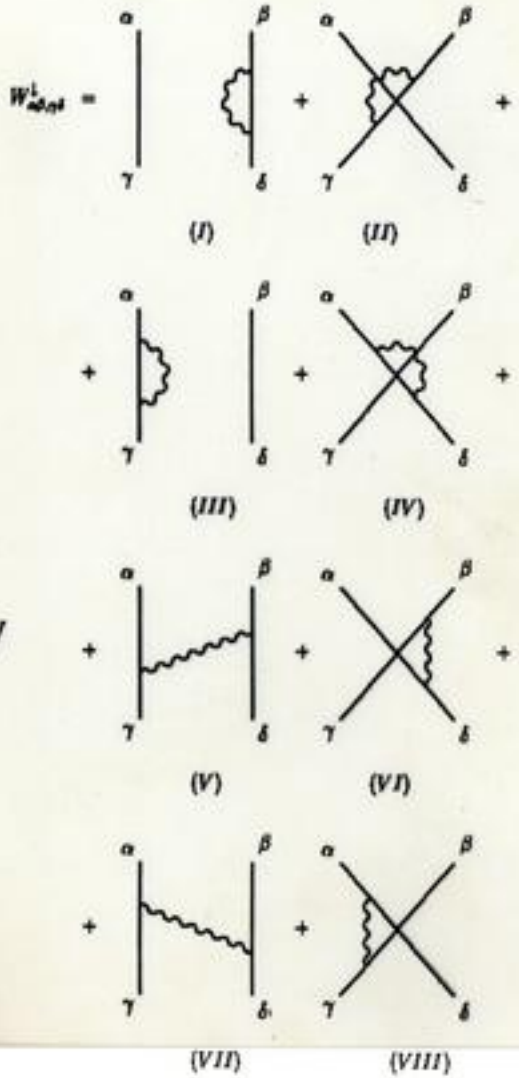

Fig. 1. Diagrams corresponding to the coupling of the 2qp configurations to the more complicated states including a phonon. See Section 2 for the discussion of this coupling, the detailed analytic expressions being given in Appendix A.

$$S(E) = -\frac{1}{\pi}\,\mathrm{Im}\sum_{\nu}\frac{(\mathrm{g.s.}|\hat{F}|\nu)^2}{E - E_\nu + \mathrm{i}\Gamma_\nu/2}. \tag{2}$$

More in detail, each matrix element of $W^{\downarrow}(E)$ written in the basis of the discrete QRPA states is a linear combination of matrix elements $W^{\downarrow}_{\alpha\beta,\gamma\delta}(E)$ in the basis of the 2qp configurations $(\alpha\beta)$, $(\gamma\delta)$, etc. These latter matrix elements are sums of the eight terms depicted in Fig. 1. To evaluate these diagrams, we employ the following expression for the particle–vibration coupling Hamiltonian:

$$V = \sum_{\alpha\beta}\sum_{LnM}\langle\alpha|\varrho^{(L)}_n(r)v(r)Y_{LM}(\hat{r})|\beta\rangle a^{\dagger}_{\alpha}a_{\beta}, \tag{3}$$

and we use the standard BCS expressions to relate the quasiparticle operators $c^{\dagger}_{\alpha}$ and c_{α} to the single-particle ones $a^{\dagger}_{\alpha}$ and a_{α} (see Eq. (13)). In Eq. (3) the vibration (phonon) $|n\rangle$ is characterized by its angular momentum L and its transition density $\varrho^{(L)}_n(r)$, while the form factor $v(r)$ is related to the particle–hole interaction V_{ph} derived from the Skyrme force as $V_{\mathrm{ph}}(\vec{r}_1,\vec{r}_2) = v(r_1)\delta(\vec{r}_1 - \vec{r}_2)$. The detailed expressions of the diagrams are given in Appendix A.

3. Application to the dipole response of $^{18\text{–}22}$O

We use the model discussed above to calculate the electric dipole strength distributions in the unstable neutron-rich oxygen isotopes. As anticipated in the introduction, in a recent experiment [17] at GSI its knowledge has been extended to the isotopes heavier than ^{18}O, for which it was well known [38,39], with systematic measurements from $A = 17$ to $A = 22$. Low-energy strength was detected, which exhausts up to 12% of the classical Thomas–Reiche–Kuhn (TRK) energy-weighted sum rule (EWSR) at excitation energies

below 15 MeV (approximate
detected in the experiment). Th
for our model.

The calculations have been
force SIII [35]. This force, in
energy of these nuclei (althoug
the corresponding self-consist
poor in the comparison with t
some pairing correlations [18,
matrix elements of strength G
the corresponding values of
pairing gaps are smaller than
and the binding energies differ
the low-lying 2^+ states are so
case of ^{20}O, the experimental
about 3 e^2 fm^4 and our QRP
large values of the pairing gap

The HF–BCS calculations
extending up to 15 fm. The
(high-lying states acquire lar
the single-particle space, in s
interaction: in our case, the
calculations for the dipole an
the residual interaction betw
including the pairing contrib
2^+, 3^- and 4^+ which lie be
In the case of ^{18}O, the 0^+ m
small. On the other hand, th
effective in producing the d
less important due to energy

The quasiparticle states c
above the Fermi energy, up
250, respectively in the 1^-
model space does not alter
is large enough so that the
dipole case, the total photo
σ_{tot}) which is proportional
exhausted by the QRPA cal
and the ratio between the tw

[1] These $B(E2)$ values are obtain
RPA and its extensions, the use of

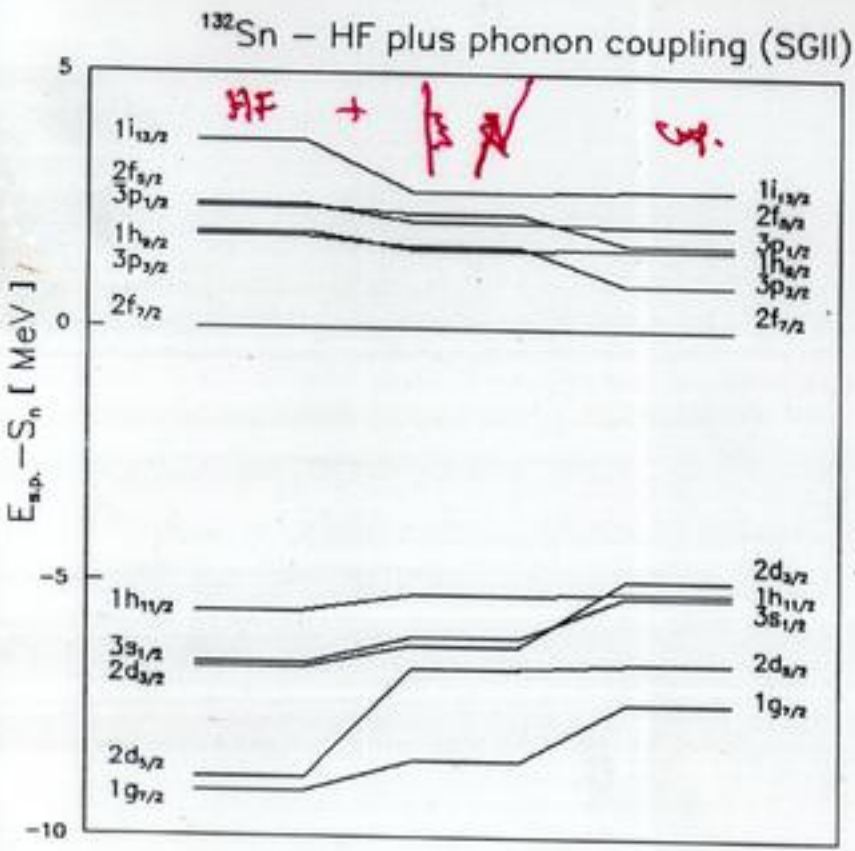

Spec. factors	
1i 13/2	0.72
2f 5/2	0.90
3p 1/2	0.95
1h 9/2	0.91
3p 3/2	0.93
2f 7/2	0.91
2d 3/2	0.90
1h 11/2	0.89
3s 1/2	0.91
2d 5/2	0.61
1g 7/2	0.83

HF + BCS (^{100}Sn)

$$V_{pair.}(\vec{r}_1, \vec{r}_2) = -640\,(\text{MeV fm}^3)\left[1 - P\left[\rho_0\right]\right]\delta(\vec{r}_1 - \vec{r}_2)$$

5 s.p. states $1h_{11/2}, 2f_{7/2}, 1h_{9/2}, 1i_{13/2}, 3p_{3/2}$

- box, 25 fm, $\Delta r = 0.1$ fm.
- (R)RPA 2 g.s. energies $\leq$ 100 MeV
- 1^- at zero energy $\rightarrow$ $1.05\,V_{ph}$
- 0^+ at " " 0.K. (^{100}Sn)
- in the PV coupling 2^+, 3^-, 4^+, 1^- with $\hbar\omega \leq$ 30 MeV, strength $\geq 5\%$

D. Sarchi, PFB, G. Colò, [redacted].

PLB 601 (2004) 27.

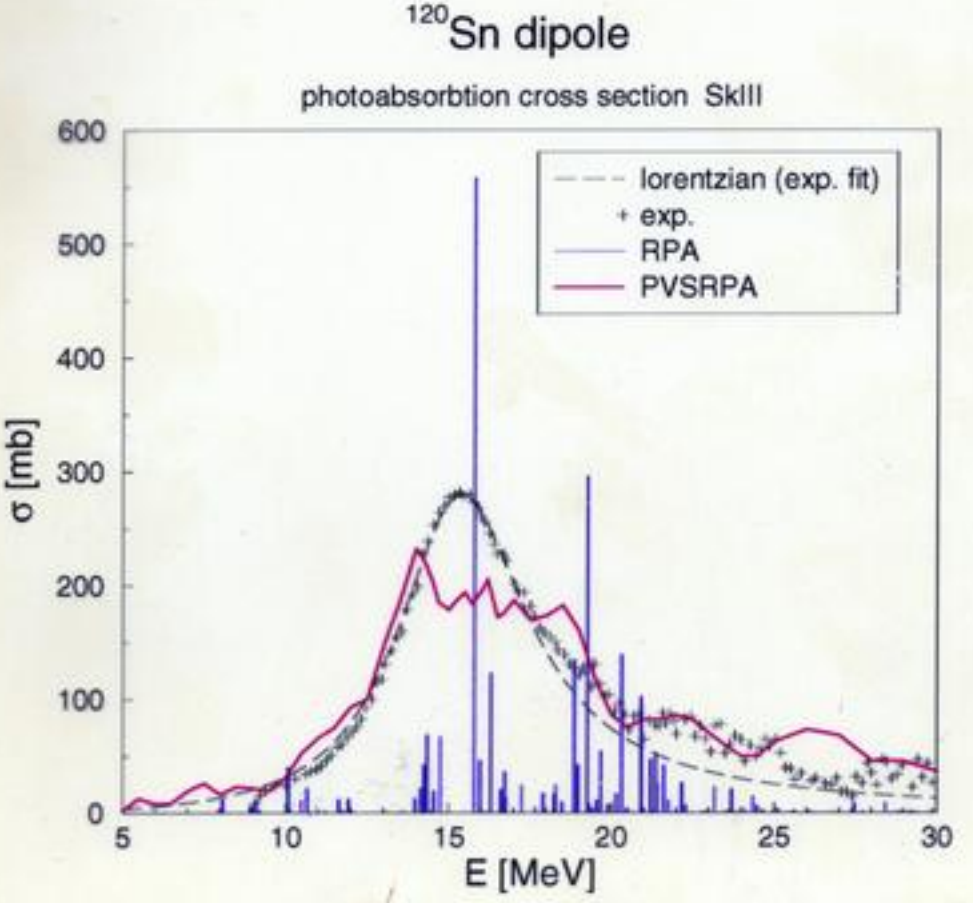

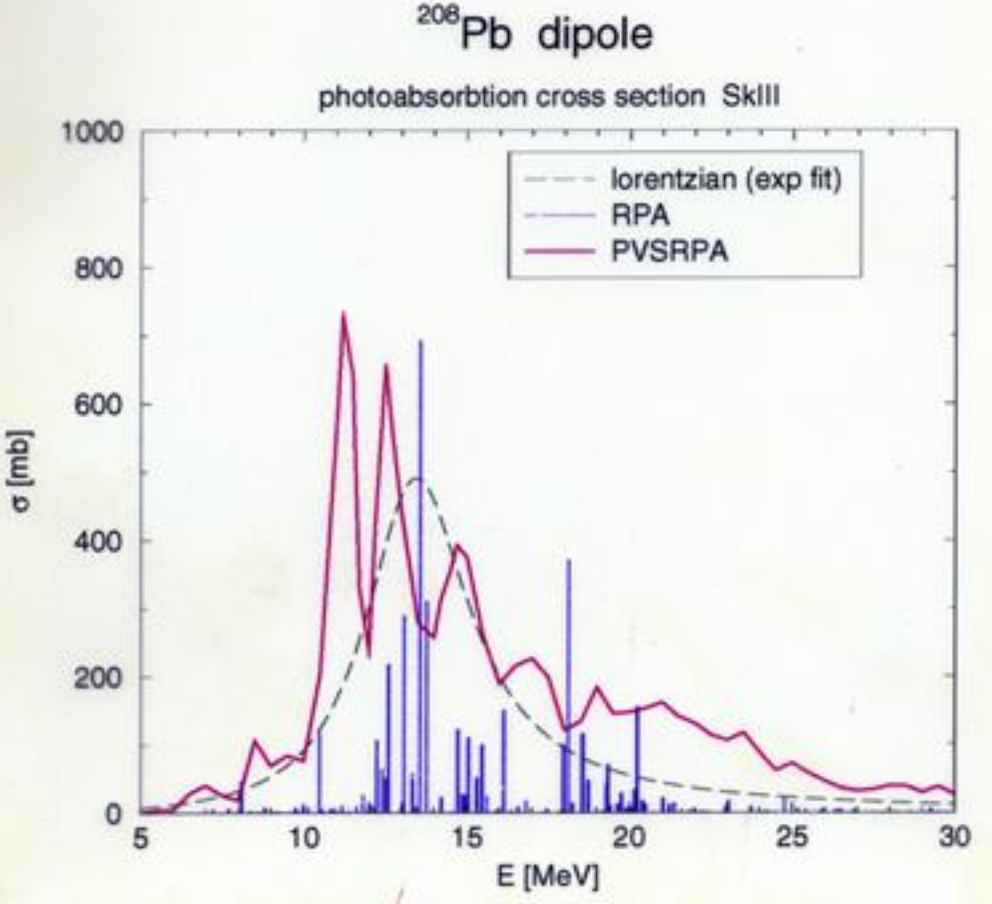
^{208}Pb dipole
photoabsorbtion cross section SkIII
lorentzian (exp fit)
RPA
PVSRPA
σ [mb]
E [MeV]
0
200
400
600
800
1000
5
10
15
20
25
30

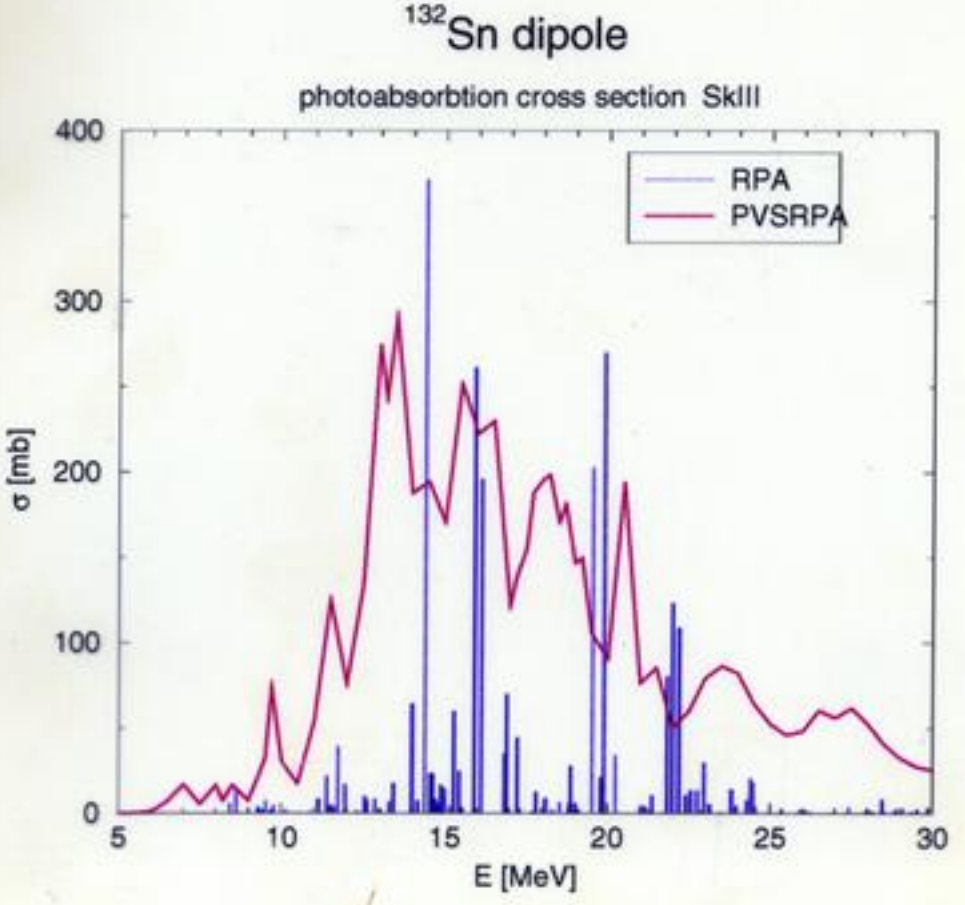
^{132}Sn dipole
photoabsorbtion cross section SkIII
RPA
PVSRPA
σ [mb]
E [MeV]
0
100
200
300
400
5
10
15
20
25
30

Table 1
Centroid energies $E_0 = m_1/m_0$ obtained within RPA or QRPA (together with the unperturbed HF or HF-BCS result in parenthesis), compared with the empirical prediction $80\,A^{-1/3}$ ($41\,A^{-1/3}$)

Nucleus	SIII	SLy4	$80\,A^{-1/3}$ ($41\,A^{-1/3}$)
^{208}Pb	14.9 (9.4)	13.4 (9.8)	13.5 (6.9)
^{120}Sn (RPA)	17.1 (10.9)	15.0 (11.0)	16.2 (8.3)
^{120}Sn (QRPA)	17.3 (11.3)	15.1 (11.6)	16.2 (8.3)
^{132}Sn	17.0 (10.7)	15.2 (11.0)	15.7 (8.1)

Table 2
Centroid energies $E_0 = m_1/m_0$ in MeV, obtained in the (Q)RPA and (Q)RPA–PC calculations. Only in the case of ^{208}Pb we observe an appreciable shift when the phonon coupling is introduced. In the other two cases the downward shift is smaller than 100 keV

Nucleus	(Q)RPA	(Q)RPA–PC
^{208}Pb	14.9	14.4
^{120}Sn	17.1	17.1
^{132}Sn	17.0	17.0

the repulsive matrix elements obtained with SIII are systematically larger that those of the SLy4. From the comparison between RPA and QRPA results for the nucleus ^{120}Sn, we can deduce that the pairing interaction does not play a crucial role, as expected.

In Table 2, the results for the centroid energy without and with the phonon coupling are shown. In the case of ^{208}Pb, the centroid energy after the coupling is 14.4 MeV, to be compared with the value 14.9 MeV at the level of RPA. In the case of ^{120}Sn, the centroid energy, at the level of the complete calculation is the same value of the QRPA calculation. The same is true for ^{132}Sn.

The integral of the strength as a function of the upper integration limit, that is, the cumulated value of the EWSR, is shown in Fig. 1. This cumulated value is shown as a fraction of the total expected value, which is the TRK sum rule multiplied by the enhancement factor $(1 + \kappa)$. The values of the total EWSR in MeV fm^2 (and of κ in parenthesis) are, for ^{120}Sn, ^{132}Sn and ^{208}Pb, respectively: 2448 (0.399), 2566 (0.397) and 4202 (0.408). One can see that, in order to exhaust more than 90–95% of the EWSR in the (Q)RPA–PC calculation, one has to reach 30 MeV in the case of ^{208}Pb and 40 MeV in the case of the Sn isotopes. We stress that, while the shape of the strength distribution and the GDR peak position change when

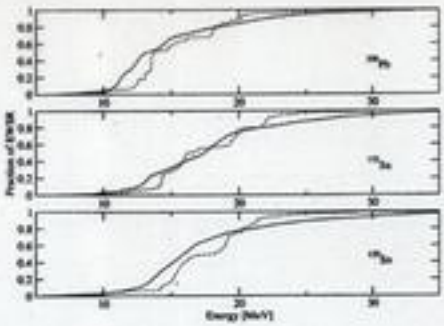

Fig. 1. Exhaustion of the dipole EWSR in the three nuclei considered in the present Letter. The full line refers to the complete (Q)RPA calculation, while the dashed line to the (Q)RPA calculation.

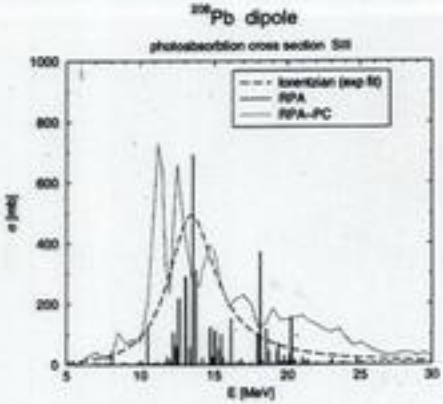

Fig. 2. Photoabsorption cross section for ^{208}Pb.

the particle-vibration coupling is taken in account, the centroid and the EWSR values are much less affected.

In Figs. 2–4, we show the calculated photoabsorption cross sections, together with the experimental results for the two stable nuclei. The values of energies and the widths obtained from a Lorentzian fit of our cross sections are summarized in Table 3.

We can see that the agreement with the experimental results is good for both ^{208}Pb and ^{120}Sn. This gives us confidence to use the model for a prediction of the photoabsorbtion in the unstable nucleus ^{132}Sn. In this

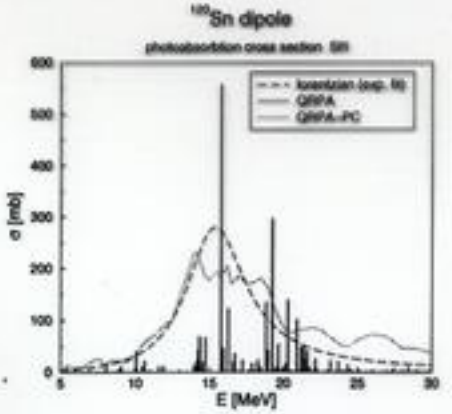

Fig. 3. Photoabsorption cross section for ^{120}Sn.

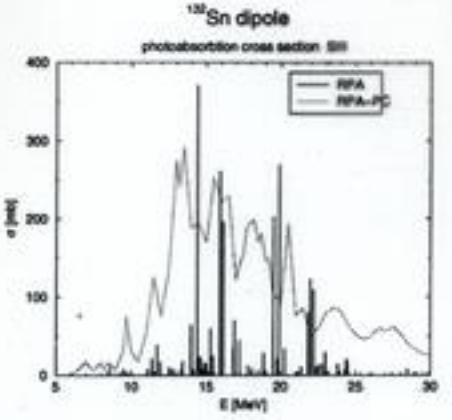

Fig. 4. Photoabsorption cross section for ^{132}Sn.

Table 3
Values of the peak energy (width) in MeV calculated in (Q)RPA–PC (calculated by means of a Lorentzian fit to the cross sections) in comparison with the experimental values

Nucleus	(Q)RPA–PC	Exp.
^{208}Pb	13.1 (3.7)	13.46 (3.9)
^{120}Sn	15.7 (5.3)	15.4 (4.9)
^{132}Sn	15.5 (5.8)	

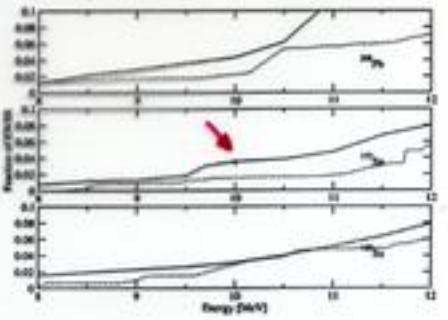

Fig. 5. Low-lying dipole strength in the three isotopes studied. The figure has the same pattern of Fig. 1, but it refers only to the interval 8–12 MeV.

case the width is about 6 MeV, like in ^{120}Sn, but the cross section is very fragmented.

In the low-lying energy region, we obtain strength in the three nuclei, as we discuss below. The cumulated value of the EWSR below 12 MeV is shown in Fig. 5. For ^{208}Pb, a comparison is possible with the data of Ref. [9]. Our calculation gives a total integrated strength $B(E1) = 0.53\ e^2\,fm^2$ (below 6 MeV) and $B(E1) = 1.27\ e^2\,fm^2$ (up to 8 MeV), whereas the experimental data are $B(E1) = 0.52\ e^2\,fm^2$ (below 6 MeV) and $B(E1) = 0.80\ e^2\,fm^2$ (up to 8 MeV). The states carrying this strength are mainly single-particle excitations, so the value of their energy is affected by the single-particle energy spectrum. On the other hand, the global B(E1) distribution is well reproduced qualitatively and quantitatively.

Coming to the Sn isotopes, the low-lying dipole strength grows faster, at the level of (Q)RPA, in ^{120}Sn. The phonon coupling affects more ^{132}Sn, reversing somewhat the trend. Also from Figs. 4 and 3 one can see that in ^{132}Sn four definite peaks exhaust the strength below 10 MeV, whereas in ^{120}Sn only a kind of smooth background is visible.

We have analyzed the structure of the four lying below 10 MeV in ^{132}Sn. In RPA, the lowest peak at 8.44 MeV is mainly (78%) associated with the $3s_{1/2} \to 3p_{3/2}$ single-particle transition, and absorbs only 0.2% of the EWSR. There are two higher peaks which lie at 8.61 and 9.53 MeV and absorb respectively 0.5% and 0.3% of the EWSR: they involve an admixture of the $2d_{3/2} \to 3p_{1/2}$ and $3s_{1/2} \to 3p_{1/2}$

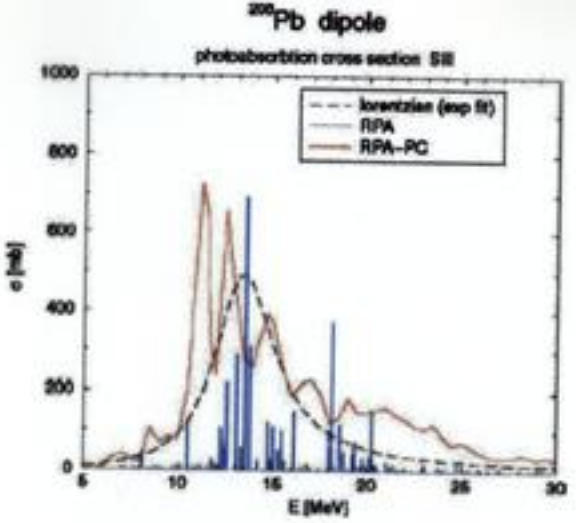

Fig. 2. Photoabsorption cross section for ^{208}Pb.

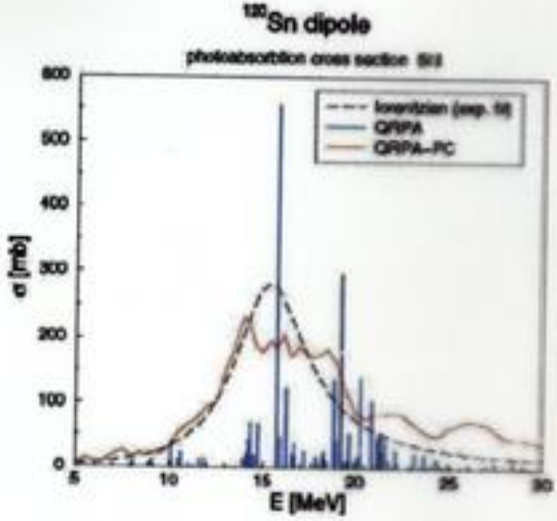

Fig. 3. Photoabsorption cross section for ^{120}Sn.

Σ B(E1) in e^2fm^2		
	< 6 MeV	< 8 MeV
Exp.*	0.53	0.80
Th.	0.52	1.27

*N. Ryezayeva et al., PRL 89 (2002) 272502

D. Sarchi *et al.* PLB 601 (2004) 27.

(QRPA-PC)

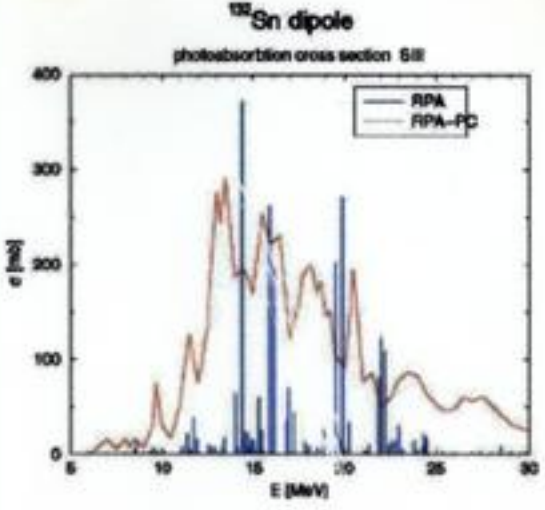

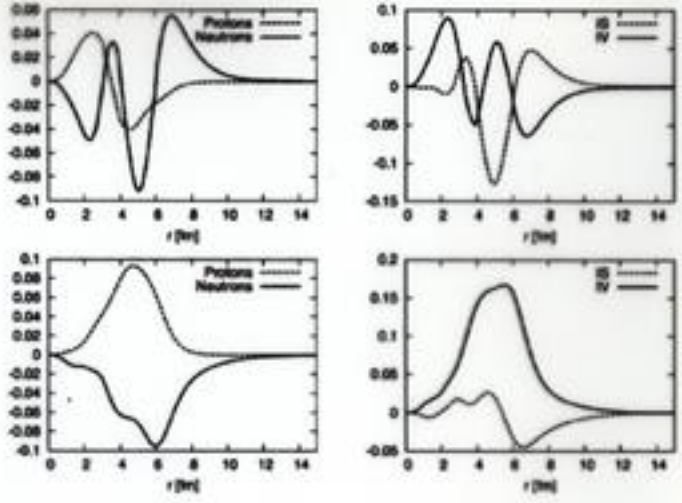

At low energy, there is not a single "collective" pygmy state

8.44 MeV $3s_{1/2} \rightarrow 3p_{1/2}$ 0.2%

8.61 MeV $2d_{3/2} \rightarrow 3p_{1/2}$, $3s_{1/2} \rightarrow 3p_{1/2}$ 0.5%

9.53 MeV 0.3%

Università degli Studi di Milano Dipartimento di Fisica

INFN Istituto Nazionale di Fisica Nucleare

RRPA

Table 3
Distribution of neutron particle–hole configurations for the states at 9.0 MeV (4.3% EWSR) in ^{68}Ni (left column), and at 8.6 MeV state (1.4% EWSR) in ^{132}Sn (right column)

^{68}Ni at 9.0 MeV	^{132}Sn at 8.6 MeV
(26.1% $1f_{5/2} \rightarrow 2d_{5/2}$)	(28.2% $2d_{3/2} \rightarrow 2f_{5/2}$)
(22.9% $2p_{3/2} \rightarrow 2d_{5/2}$)	(21.9% $2d_{5/2} \rightarrow 2f_{7/2}$)
(11.3% $1f_{7/2} \rightarrow 1g_{9/2}$)	(19.7% $2d_{3/2} \rightarrow 3p_{1/2}$)
(10.3% $2p_{1/2} \rightarrow 2d_{3/2}$)	(10.5% $1h_{11/2} \rightarrow 1i_{13/2}$)
(10.0% $1f_{5/2} \rightarrow 2d_{3/2}$)	(3.5% $2d_{5/2} \rightarrow 3p_{3/2}$)
(8.2% $2p_{3/2} \rightarrow 3s_{1/2}$)	(1.9% $1g_{7/2} \rightarrow 2f_{5/2}$)
(1.4% $2p_{1/2} \rightarrow 3s_{1/2}$)	(1.5% $1g_{7/2} \rightarrow 1h_{9/2}$)
(1.0% $1f_{5/2} \rightarrow 1g_{7/2}$)	(0.6% $1g_{7/2} \rightarrow 2f_{7/2}$)
(0.3% $1f_{5/2} \rightarrow 3d_{3/2}$)	(0.6% $2d_{3/2} \rightarrow 3p_{3/2}$)

The percentage of a ph configuration refers to the normalization of the RRPA amplitudes (12). Only configurations which contribute more than 0.1% are displayed.

the low-energy region, which displays a more complex structure of the RRPA amplitude, i.e. a coherent superposition of more than just a few neutron ph configurations. In the case of ^{68}Ni, this is the state at 9 MeV (4.3% EWSR). The distribution of neutron ph configurations for this state is included in Table 3. A dipole state with a similar structure in ^{78}Ni is found at 8.9 MeV (4.0% EWSR). The transition densities for this state are compared with those of the GDR state at 16.4 MeV in Fig. 8. We notice that the state at 8.9 MeV is characterized by a strong isoscalar transition density and a long tail of the neutron transition density which extends almost to 10 fm.

Suzuki, Ikeda and Sato (SIS) analyzed the onset of pygmy dipole resonances in neutron-rich nuclei in the framework of the two-fluid (the core fluid and the neutron excess fluid) Steinwedel–Jensen hydrodynamical model [10]. SIS derived the following relation between the energy of the pygmy dipole resonance and the excitation energy of the GDR

$$E_{\mathrm{PR}} = \sqrt{\frac{Z(N-N_c)}{N(Z+N_c)}}\,E_{\mathrm{GDR}}, \tag{13}$$

where N_c denotes the number of neutrons that form the core together with Z protons, and N is the total number of neutrons.

In Fig. 9 (upper panel) we compare the RRPA results for the centroid energies of the GDR states in the Ni isotopes with the empirical relation $E = 78A^{-1/3}$ [31]. The centroid energies in the low-energy region below 10 MeV are compared with the hydrodynamical prediction for the excitation energies of pygmy resonances (SIS) in the lower panel (Eq. (13) with $N_c = Z$). We notice that the RRPA centroid energies are in fair agreement with the empirical mass dependence of the GDR. The SIS model predicts the position of the pygmy dipole resonance to increase with neutron excess, in contrast to the RRPA results which display the opposite behavior. This discrepancy was also noted and discussed in

GSI - LAND subm. to PRL 95 (2005) 132502

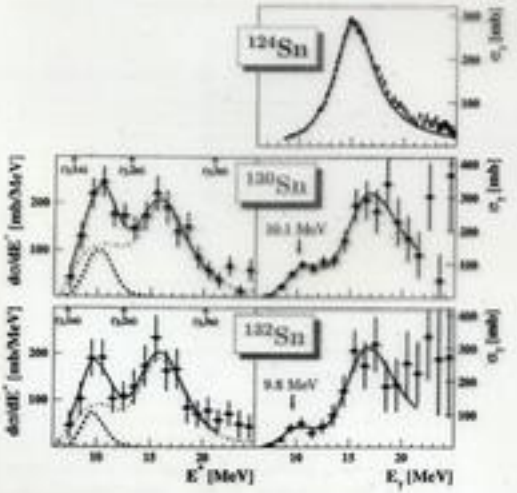

FIG. 2: (Color online) Middle and bottom left panels: energy differential electromagnetic dissociation cross sections measured in ^{130}Sn and ^{132}Sn. Arrows indicate the neutron separation thresholds. Corresponding right panels: deduced photoneutron cross sections. The curves represent fitted Gaussian (blue dashed) and Lorentzian (green dash-dotted) distributions, assigned to the PDR (centroid indicated by an arrow) and GDR, respectively, and their sum (red solid), after folding with the detector response. Top right panel: photoneutron cross section in the stable ^{124}Sn isotope measured in a real-photon absorption experiment; the solid red line represents a Lorentzian distribution [16].

then transformed back to energy-differential cross section, folded with the detector response, and its parameters are found by χ^2 minimization against the experimental data. In this way, positions, widths and integrated cross sections of both, the PDR and GDR peaks, are found. The solid (red) lines in the middle and bottom panels of Fig. 2 represent the resulting cross sections after convolution with the detector response. A summary of the deduced PDR and GDR parameters is given in Table I; data for the most neutron rich stable ^{124}Sn isotope taken from [17] are added for comparison. Parameters of the Gaussian and Lorentzian distributions adopted to describe the PDR and the GDR peaks, i.e., peak energy (E_{max}), width parameters (σ and Γ, respectively), and the integral over the photo-neutron cross section ($\int \sigma_\gamma$) are quoted. Because of the finite energy resolution, only an upper limit for the PDR width could be deduced. The errors as quoted in Table I include the correlations among all fitted parameters.

As far as the giant dipole resonance parameters are concerned, within error bars no significant deviations from that known for the stable tin isotopes or stable isotopes in the same mass region [1, 17] are observed.

	PDR			GDR		
	E_{max} [MeV]	σ [MeV]	$\int \sigma_\gamma$ [mb MeV]	E_{max} [MeV]	Γ [MeV]	$\int \sigma_\gamma$ [mb MeV]
^{124}Sn	-	-	-	15.28	4.8	2081
^{130}Sn	10.1(7)	< 1.4	130(55)	15.9(5)	4.8(1.7)	2680(410)
^{132}Sn	9.8(7)	< 2.1	78(37)	16.1(7)	4.7(2.1)	2330(590)

Theory 15.5 5.8

TABLE I: Summary of the parameters deduced for the PDR and GDR peaks. The parameters for ^{124}Sn are from [17].

The essential difference compared to the dipole strength distribution of the stable isotopes is manifested in the appearance of the low-lying component as already noticed. The integrated PDR cross section corresponds to 7(3)% and 4(3)% of the value of the Thomas-Reiche-Kuhn (TRK) energy weighted sum rule (EWSR) for ^{130}Sn and ^{132}Sn, respectively. The respective B(E1)↑ values amount to 3.2 and 1.9 e^2fm^2 or to 4.3 and 2.7 Weisskopf units (w.u.), the latter if adopting a neutron transition (for the definition of w.u. adopted here see [1]). Having in mind the well-known strong suppression, compared to the Weisskopf estimate, of E1 single-particle transitions, such large B(E1) values seem to indicate that the observed low-lying strength is either composed out of a large nymberof single-particle transitions or involves a coherent superposition of transitions forming a new collective mode. It should be remembered that the dipole strength is measured only above the one-neutron separation threshold and thus only part of the low-lying strength may be covered in the present experiment. In fact, recent real-photon measurements on stable N=82 isotones [9] revealed a concentration of E1 strength in bound states below the neutron threshold spread over excitation energies between 5.5 and 8 MeV and exhausting, however, less than 1% of the EWSR. Real photon scattering experiments to bound states of the stable isotopes ^{116,124}Sn show a concentration of E1 strength around 6.5 MeV with B(E1) values, however, of only 0.20 and 0.35 e^2fm^2, respectively [?]. A preliminary analysis of the odd ^{129,131}Sn isotopes contained in the beam cocktail of the present experiment indicates that the E1 strength extends down to lower excitation energies; the one-neutron separation energy in these odd isotopes is about 2 MeV lower than in the even ^{130,132}Sn isotopes.

	this exp.	RRPA	RPA-PC
^{130}Sn	0.05(2)	0.055	-
^{132}Sn	0.03(2)	0.05	0.04

TABLE II: Ratio of the photoneutron cross section of the PDR to that of the GDR from this experiment in comparison to the microscopic calculations [4] (RRPA) and [5] (RPA-PC)

Recently, the dipole strength distribution in neutron-rich Sn isotopes was theoretically investigated in relativistic (quasiparticle) random phase approximation (RRPA) [4?

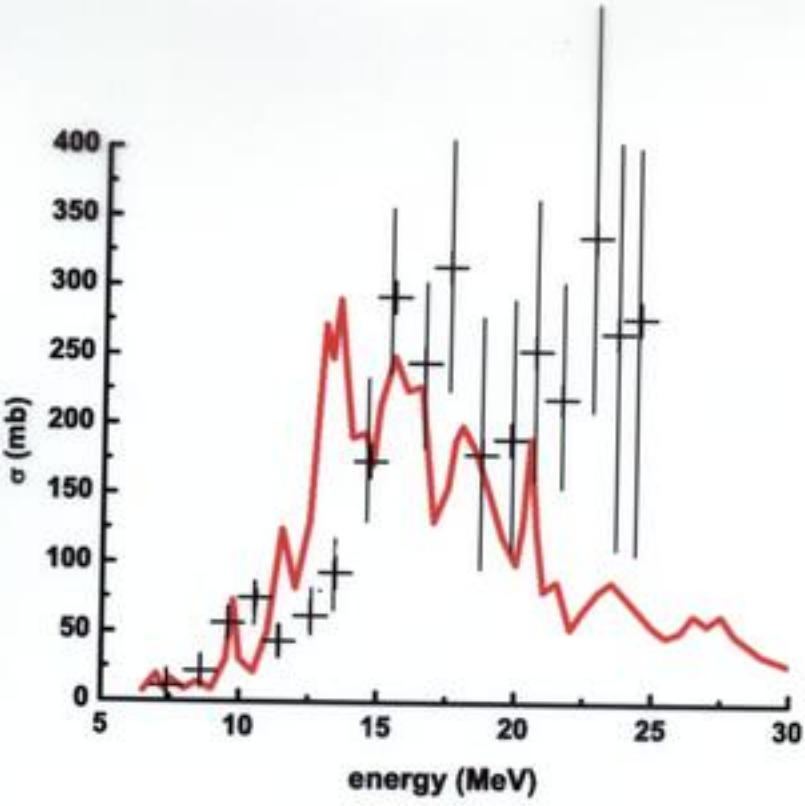

Fig. 1.

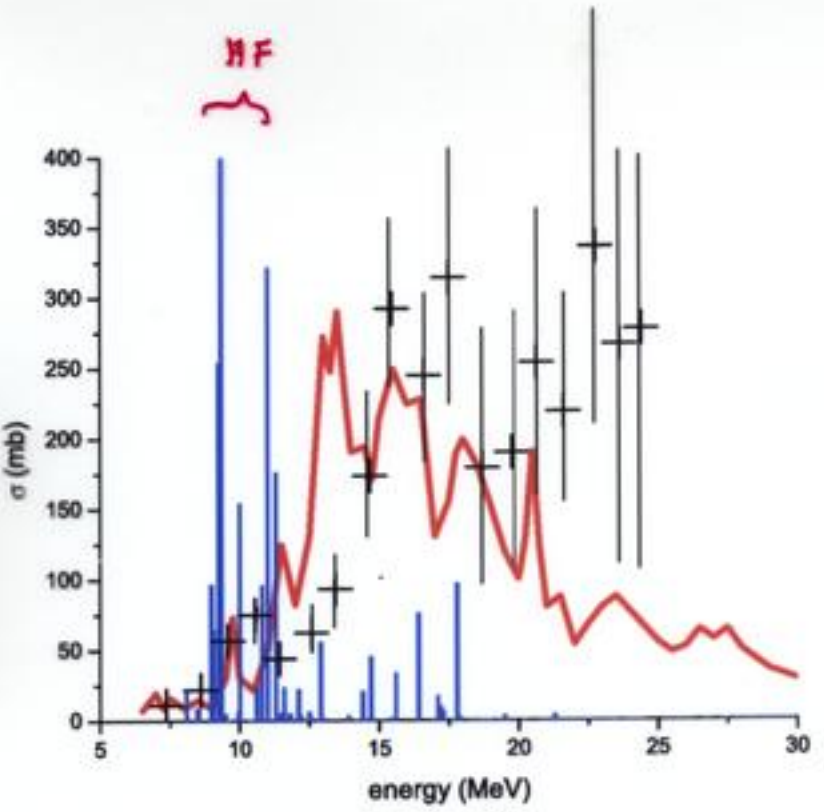

Fig. 1.

Screening ??

See H. Sagawa, H. Esbensen NPA 693 (2001) 448

Book of George and Ricardo

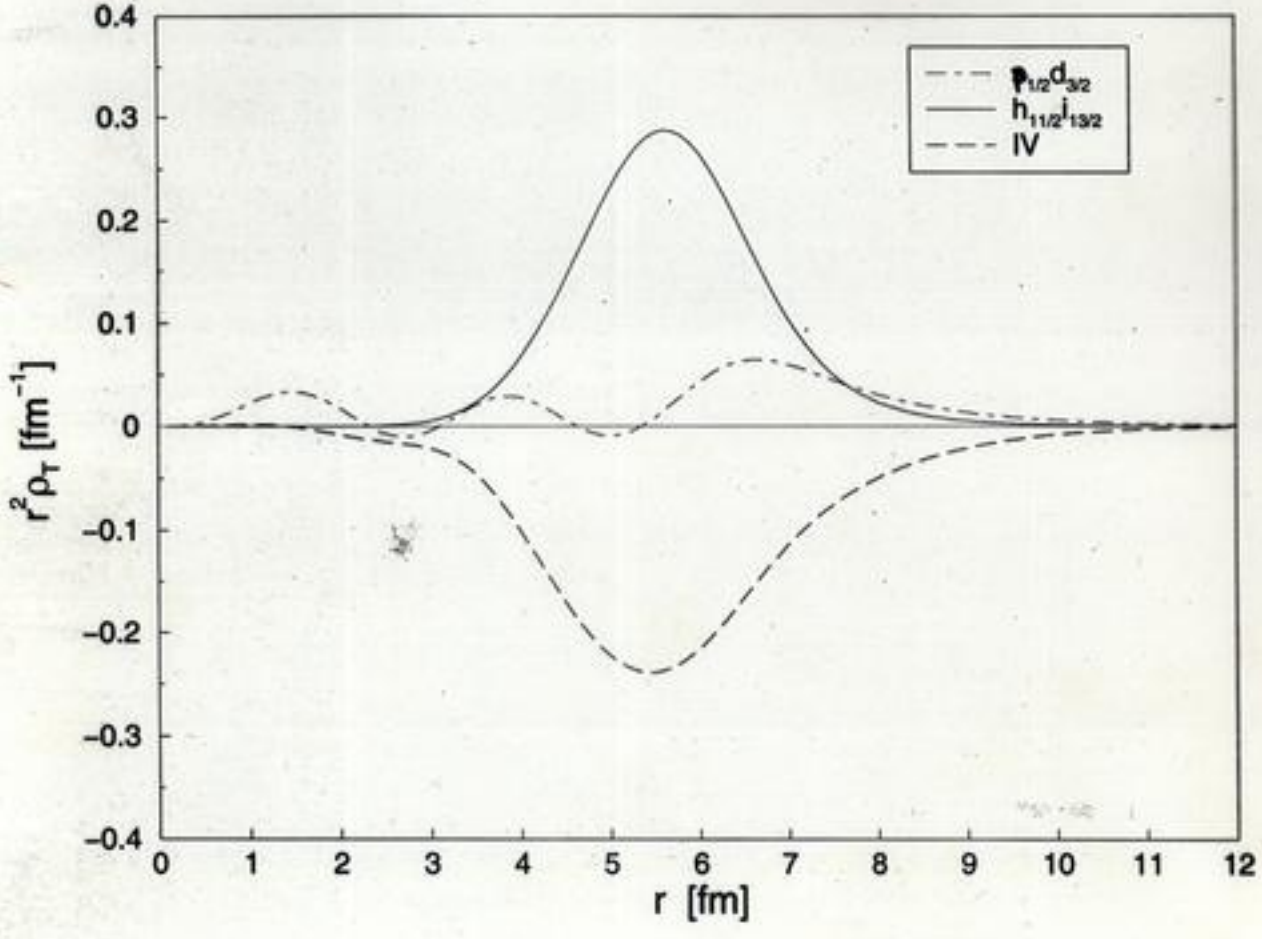

ISGQR	D1S'	$64A^{-1/3}$	Exp.
^{78}Ni	15.94	14.98	
^{100}Sn	15.13	13.79	
^{132}Sn	13.79	12.57	
^{208}Pb	11.98	10.80	10.60

Table 3: Mean values of ISGQR energies in MeV obtained with D1S' in the four studied nuclei compared with the empirical $64A^{-1/3}$ law and the ^{208}Pb experimental value from Ref. [2].

			Experiment	
2_1^+	E	B(E2)	E(MeV)	B(E2)
^{78}Ni	2.73	466		
^{100}Sn	3.84	1431		
^{132}Sn	3.97	1134	4.041	1400 (600)
^{208}Pb	4.609	2781	4.08	3180 (160)

Table 4: Energies in MeV and corresponding B(E2) in e^2fm^4 of 2_1^+ states calculated with the D1S' interaction. Existing experimental data from Refs. [24] and [25] are also listed.

2_1^+	(1)		(2)		(3)		(tot)	
	E	B(E2)	E	B(E2)	E	B(E2)	E	B(E2)
^{78}Ni	3.53	257	2.84	456	3.43	271	2.73	466
^{100}Sn	4.64	1103	3.95	1552	4.48	1041	3.84	1431
^{132}Sn	4.61	775	4.04	1182	4.53	770	3.97	1134
^{208}Pb	5.15	2305	4.65	3145	5.09	2123	4.61	2781

Table 5: Energies in MeV and B(E2) of 2_1^+ states obtained by leaving out from the D1S' p-h interaction: (1) the spin-orbit and the Coulomb terms, (2) the Coulomb term, (3) the spin-orbit term, (tot) no term.

S. Peru, J. F. Berger and PFB nucl-th/0506022, EPJA in prep.

Table 9. Summed electric dipole and quadrupole strength in Ca isotopes between 5 and 10 MeV

		^{40}Ca	^{44}Ca	^{48}Ca
$\Sigma B(E1)\uparrow$, 10^{-3} e^2 fm^2	Exp.	5.1(8)	89	55.7(41)
	ETFFS	17	220	111
	CQRPA	27	129	327
$\Sigma EB(E1)\uparrow$, keV e^2 fm^2	Exp.	34.7(55)		467.0(350)
	ETFFS	120	1605	967
	CQRPA	251	967	2806
$\Sigma B(E2)\uparrow$, e^2 fm^4	Exp.	332(60)		407(32)
	ETFFS	564	337	562
	CQRPA	349	371	220
$\Sigma EB(E2)\uparrow$, MeV e^2 fm^4	Exp.			
	ETFFS	4196	2424	4748
	CQRPA	3227	3174	1792

Table 10α. Summed electric dipole strength in Sn isotopes below 10 MeV

	Model	^{104}Sn	^{120}Sn	^{132}Sn	^{150}Sn
$\Sigma B(E1)\uparrow$, e^2 fm^2	ETFFS	3.43	6.85	3.87	7.33
	CQRPA	0.41	2.35	2.55	8.19
$\Sigma EB(E1)\uparrow$, % EWSR	ETFFS	7.29	11.7	6.52	9.20
	CQRPA	0.45	4.86	4.81	11.7

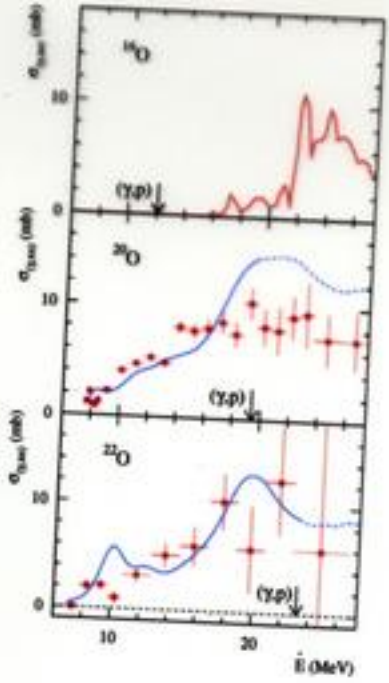

Figure 1.7: Photo-neutron cross sections measured for the unstable oxygen isotopes ^{20,22}O in comparison to that of the stable isotope ^{18}O. The blue curves show the result of a large-scale shell-model calculation [30]. The (γ,p) thresholds are indicated by arrows. Adapted from [29].

GSI data, LAND

Large-amplitude motion

To further understand the dynamical properties of the two-component nuclear matter, large-amplitude motions can be studied. *Nuclear fission* is best suited to determine the *dynamical properties of cold and moderately excited nuclear matter*. At low excitation energies, the onset of dissipation and the influence of quantal effects on large-amplitude collective motion can be studied. Nuclear fission is also a unique tool to explore shell effects at extreme deformations. Fission probabilities yield rather direct information on nuclear level densities. At higher excitation energies, the value of the nuclear viscosity can be extracted from the fission decay width compared to particle evaporation and from other observables of the fission process. First-generation experiments performed at GSI have proven that the use of secondary beams greatly enlarges the prospects of this field. So far, 70 short-lived neutron-deficient nuclei above lead have become available for fission studies, and more than 100 will be accessible in the future.

In addition to its significance for basic research, the general understanding of nuclear fission has become an essential topic in several applications. The characteristics of fission in a wide regime of excitation energies and for a large variety of nuclei are important for the lay-out of spallation neutron sources and of accelerator-driven

Cross section integrated up to 15 MeV

Experiment: A. Leistenschneider *et al.* [Phys. Rev. Lett. 86, 5442 (2001)]

Theory: G. Colò and P.F. Bortignon: QRPA + phonon coupling
[Nucl. Phys. A 696, 427 (2001)]

H. Sagawa and T. Suzuki: large scale shell model
[Phys. Rev. C 59, 3116 (1999)]

The coupling with 4qp shifts strength down.

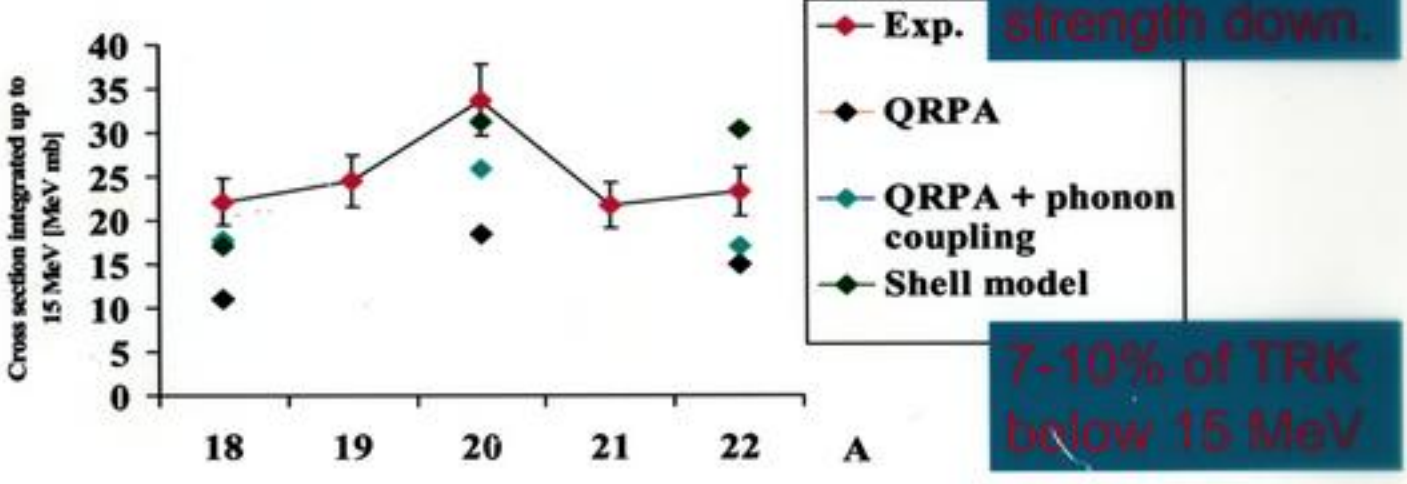

7-10% of TRK below 15 MeV

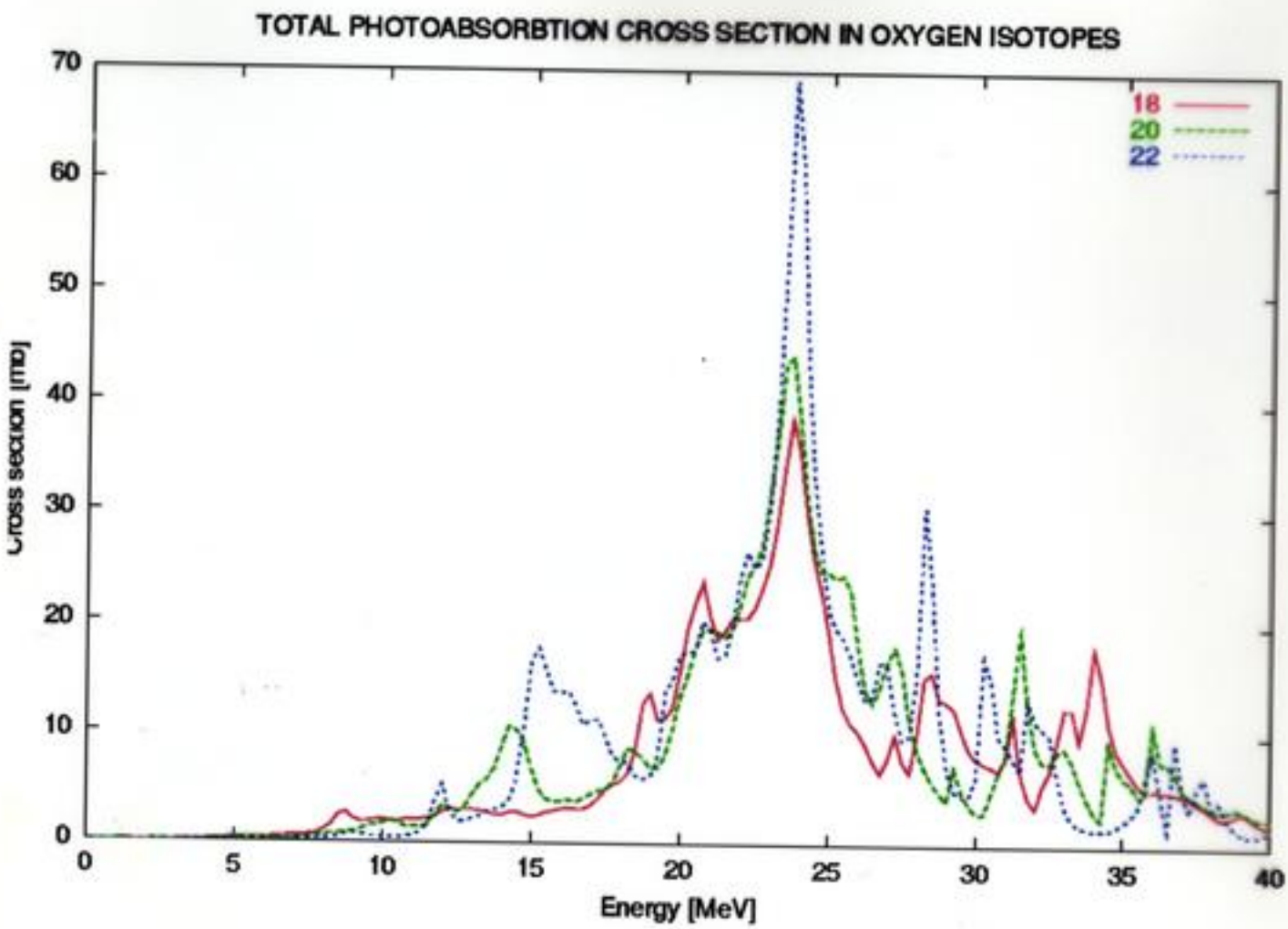
TOTAL PHOTOABSORBTION CROSS SECTION IN OXYGEN ISOTOPES
18
20
22
Cross section [mb]
Energy [MeV]
0
10
20
30
40
50
60
70
0
5
10
15
20
25
30
35
40

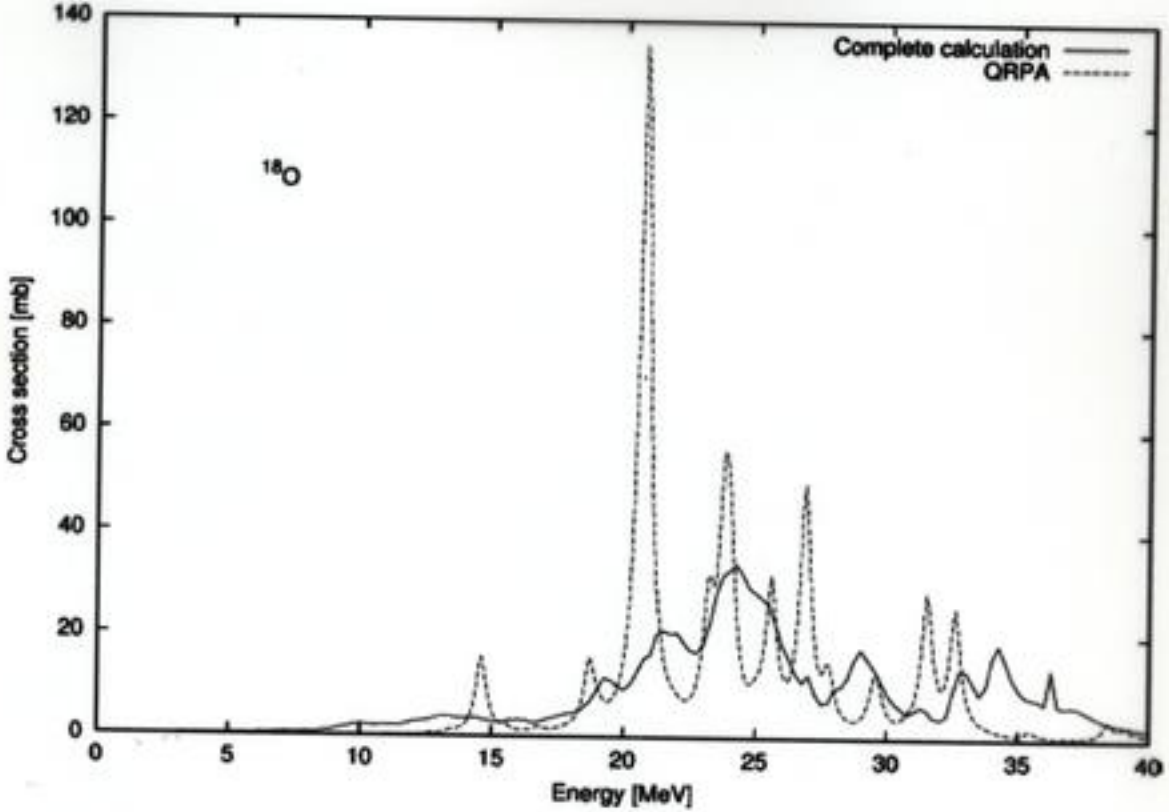
Complete calculation
QRPA
^{18}O
Cross section [mb]
Energy [MeV]
0
20
40
60
80
100
120
140
0
5
10
15
20
25
30
35
40

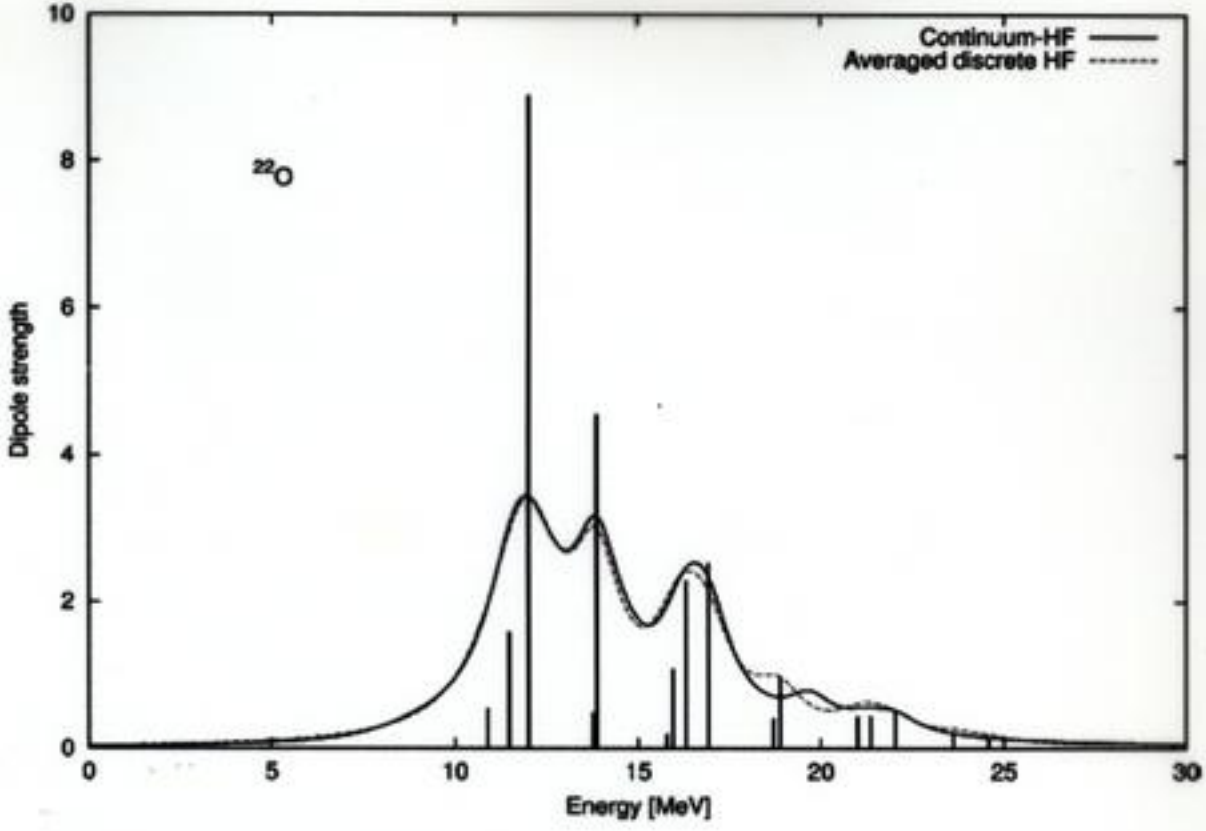
Continuum-HF
Averaged discrete HF
^{22}O
Dipole strength
Energy [MeV]
0
2
4
6
8
10
0
5
10
15
20
25
30

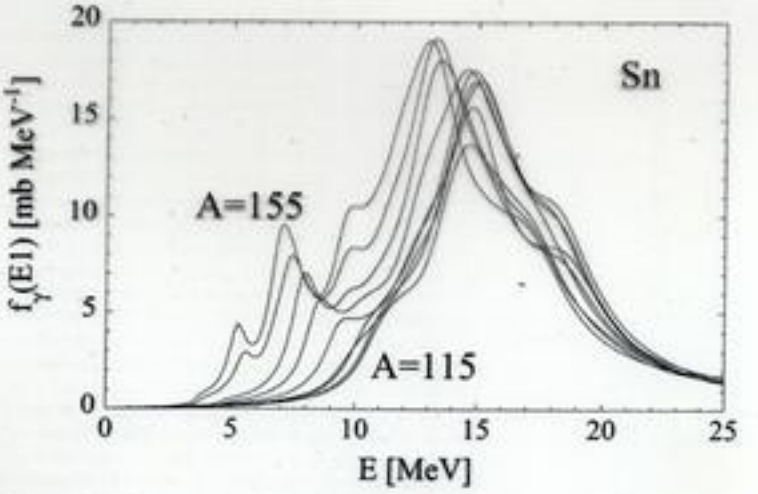

Fig. 8. E1-strength function for the Sn isotopic chain predicted by the HFB+QRPA with the BSk7 force. The SRPA is applied to all distribution. Only isotopes ranging between A=115 and A=150 by steps of ΔA=5 are displayed.

sion makes use of the nuclear ground state properties derived coherently from the same microscopic HFB method with the BSk7 Skyrme force [20]. It also benefits from the improved nuclear level density prescription based on the microscopic statistical model, also used to estimate the nuclear temperature in Eq. (17) [37]. The direct capture contribution as well as the possible overestimate of the statistical predictions for resonance-deficient nuclei are effects that could have an important impact on the radiative neutron captures by exotic nuclei [1], but are not included in the present study. The Maxwellian-averaged radiative neutron capture rate at a temperature T = 1.5 10^9 K, typical of the r-process nucleosynthesis, obtained with the QRPA E1-strength are compared in Fig. 9 with those based on the Hybrid Lorentzian-type formula [1]. These rates are sensitive to the neutron capture cross section at incident energies around 130 keV, and therefore depend on the E1 strength in a narrow range of a few hundred keV around S_n. The temperature-dependent Hybrid formula corresponds to a generalization of the energy- and temperature-dependent Lorentzian formula including an improved description of the E1-strength function at energies below S_n as derived from [3]. The Hybrid E1 strength differs from the QRPA estimate not only in the location of the centroid energy, but also in the low-energy tail. No extra low-lying strength is included in the phenomenological Hybrid formula, but its temperature dependence increases the E1 strength at low energies and is responsible for its non-zero $E \rightarrow 0$ limit. The newly-derived strength gives an increase of the rate by a factor up to 6 close to the neutron drip line. R-process nuclei characterized by $S_n \lesssim 3$ MeV are seen to have a neutron capture rate about at least twice faster than the one predicted with the phenomenological Hybrid formula. This is due to the shift of the GDR to lower energies compared with the usually adopted liquid-drop $A^{-1/3}$ rule, as well as to the appearance of

S. Goriely et al., NPA 739(2004) 331

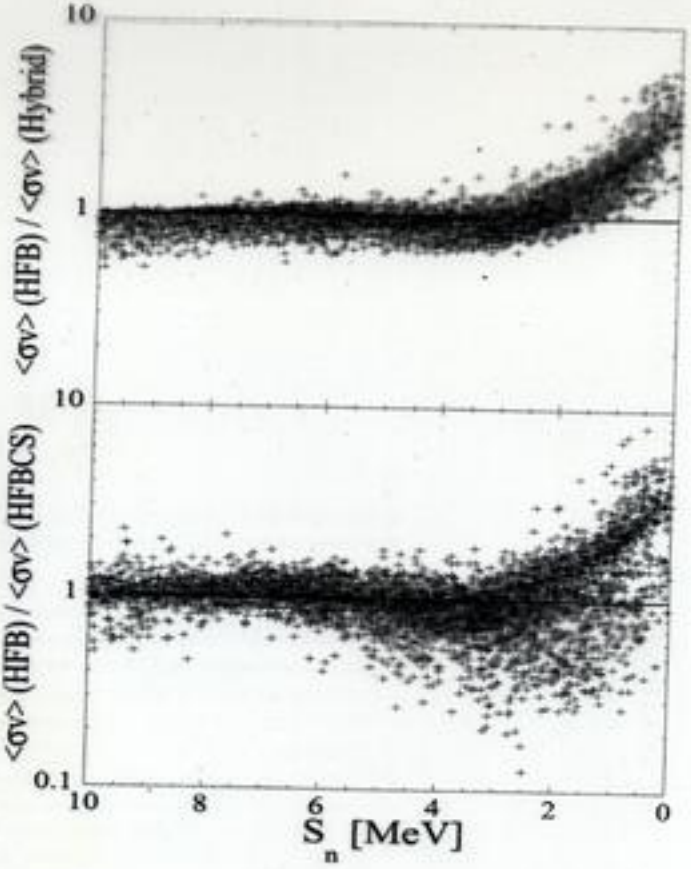

Fig. 9. Upper panel: Ratio of the Maxwellian-averaged (n,γ) rate (at a temperature of 1.5 10^9 K) obtained with the HFB+QRPA E1 strength to the one using the Hybrid formula [1] as a function of the neutron separation energy S_n for all nuclei with $8 \leq Z \leq 110$. Lower panel: Same as upper panel where the HFB+QRPA neutron capture rates are compared with the HFBCS+QRPA rates of [7].

References

[1] S. Goriely, Phys. Lett. B436 (1998) 10.

[2] C.M. McCullagh, M.L. Stelts, R.E. Chrien, Phys. Rev. C23 (1981) 1394.

[3] S.G. Kadmenskii, V.P. Markushev, V.I. Furman, Sov. J. Nucl. Phys. 37 (1983) 165.